Check for updates

High Power Laser Science and Engineering, (2025), Vol. 13, e78, 9 pages.
doi:10.1017/hpl.2025.10060

HIGH POWER LASER SCIENCE AND ENGINEERING

RESEARCH ARTICLE

General structured light generation based on a programmable linearly polarized mode synthesizer

Wei Chen[1,†], Fang Ren[2,†], Yuyang Gao[1,2], Xiaofeng Li[1], Dawei Ge[1], Zhangyuan Chen[1], Yongqi He[1], and Juhao Li[1,3]

[1] *State Key Laboratory of Advanced Optical Communication Systems and Networks, Peking University, Beijing, China*

[2] *School of Computer and Communication Engineering, University of Science and Technology Beijing, Beijing, China*

[3] *Peng Cheng Laboratory, Shenzhen, China*

(Received 31 January 2025; revised 28 May 2025; accepted 22 July 2025)

Abstract

Fiber-based structured light including cylindrical vector beams (CVBs) and orbital angular momentum (OAM) has gained significant interest for its unique properties. In this work, we propose the concept of a programmable linearly polarized (LP)-mode synthesizer for general structured light generation, in which an LP-mode pool supporting independent and selectable LP-mode output is first established, and then different CVB/OAM modes could be generated in a general way through polarization and phase control. We demonstrate a proof-of-concept LP-mode synthesizer based on a fiber ring laser characterized by a partial five-LP mode weakly coupled few-mode fiber (FMF) cavity and an arbitrary LP-mode switch array. Various CVB/OAM beams including TE_{01}, TM_{01}, $OAM_{\pm1}$ and $OAM_{\pm2}$ modes are successfully generated. This approach provides new insights into mode manipulation methods, potentially enhancing the performance of optical quantum communications, optical fiber sensing and optical trapping applications.

Keywords: cylindrical vector beam; fiber laser; mode manipulation; orbital angular momentum; structured light

1. Introduction

Maneuvering different physical dimensions of photons including frequency, time, amplitude, phase, polarization and spatial structure enables manifold light-related applications. In particular, fiber-based structured light beams such as cylindrical vector beams (CVBs) and orbital angular momentum (OAM) modes have attracted increasing attention owing to their unique properties of spatial intensity, phase and polarization distributions, which have promoted vigorous researches in optical and quantum communication systems[1,2], optical sensing[3,4], microscopy[5,6], optical trapping[7,8] and so on. For instance, the additional phase change undergone by OAM beams helps to enhance sensing resolution for interferometer applications[4].

Various approaches have been proposed to generate this structured light in recent years. Discrete components such as spatial light modulators[9,10], axial birefringent components[11], specially designed laser cavities[12–14], spiral phase plates[15,16] and plasmonic metasurfaces[17–20] have been utilized to reshape free-space Gaussian beams into CVBs/OAMs or to directly emit CVBs/OAM beams. However, the bulk volume and complex optical alignment may hinder their practical applications. Meanwhile, approaches utilizing optical fiber-based components, lasing cavities or optical circuits have also been widely investigated, such as long-period fiber gratings[21–23], vortex grating[24], mode-selective couplers (MSCs)[25,26] and tapered fiber[27]. However, the lack of a general method and extensibility to generate CVBs and OAMs may be their shared limitation.

Recent studies on the utilization of linearly polarized (LP) modes in weakly coupled FMF transmission systems may provide a new way for the generation of fiber-based structured light. In these systems[28–31], the modal crosstalk for FMFs and matched mode multiplexers/demultiplexers (MMUXs/MDEMUXs) is significantly suppressed, so that light could independently propagate through multiple LP modes and the transmission capacity could be multiplied without inter-modal multiple-input multiple-output digital signal processing. Because the effective index difference

Correspondence to: J. Li, State Key Laboratory of Advanced Optical Communication Systems and Networks, Peking University, Beijing 100871, China. Email: juhao_li@pku.edu.cn; F. Ren, School of Computer and Communication Engineering, University of Science and Technology Beijing, Beijing 100083, China. Email: renfang@ustb.edu.cn

[†]These authors contributed equally to this work.

© The Author(s), 2025. Published by Cambridge University Press in association with Chinese Laser Press. This is an Open Access article, distributed under the terms of the Creative Commons Attribution licence (https://creativecommons.org/licenses/by/4.0), which permits unrestricted re-use, distribution and reproduction, provided the original article is properly cited.

https://doi.org/10.1017/hpl.2025.10060 Published online by Cambridge University Press

($|\Delta n_{\text{eff}}|$) is the dominant factor of distributed modal crosstalk between LP modes, step-index FMF with a high core/cladding index difference and multiple-ring-core (MRC) FMF utilizing ring index perturbations to enlarge the minimum $|\Delta n_{\text{eff}}|$ among LP modes have been proposed for distributed modal crosstalk suppression[28,29]. Different kinds of MMUXs and MDEMUXs with low intrinsic channel crosstalk and coupling crosstalk have been adopted, including photonic lanterns[31,32], multiple plane light converters[33,34], volume holograms[35] and cascaded MSCs[36,37]. Further, the independent LP manipulation capability could be utilized to generate fiber-based structured light by applying proper mode conversion.

In this paper, we propose the programmable LP-mode synthesizer as a general approach to generate fiber-based structured light. An LP-mode pool is first established to generate independent and selectable LP modes. Then, different CVB/OAM modes could be generated in accordance with the conversion relation with LP modes. We experimentally demonstrate the LP-mode synthesizer utilizing a five-LP mode fiber ring laser with a partial weakly coupled FMF cavity. The output LP mode could be controlled by an arbitrary LP-mode switch array, and a polarization controller (PC) is employed for polarization and phase control. We lastly experimentally demonstrate the successful generation of various CVBs/OAM beams including TE_{01}, TM_{01}, OAM_{+1}, OAM_{-1}, OAM_{+2} and OAM_{-2}.

2. Concept of the programmable linearly polarized mode synthesizer

The conversion relations between LP modes and CVB/OAM modes are the theoretical basis for the proposed LP-mode synthesizer. As we know, the CVB modes and OAM modes are two eigenmode sets in optical fibers under the Cartesian coordinate system[38] and the circular polarization coordinate system[39], respectively. The polarization vector mode corresponds to the CVB mode, whereas the phase vortex mode conveys the OAM mode. Mathematically, the LP modes are the solutions of scalar Helmholtz equations under the weakly guiding approximation, and the superposition of near-degenerate CVB modes forms LP states. The relation of the LP modes and CVB modes could be described by the following[40]:

$$\begin{aligned}\begin{bmatrix}\mathrm{HE}^{e}_{m+1,n}\\ \mathrm{HE}^{o}_{m+1,n}\\ \mathrm{EH}^{e}_{m-1,n}\\ \mathrm{EH}^{o}_{m-1,n}\end{bmatrix} &= F_{m,n}(r)\begin{bmatrix}1&0&0&-1\\0&1&1&0\\1&0&0&1\\0&-1&1&0\end{bmatrix}\begin{bmatrix}\vec{e}_x\cos(m\varphi)\\ \vec{e}_y\cos(m\varphi)\\ \vec{e}_x\sin(m\varphi)\\ \vec{e}_y\sin(m\varphi)\end{bmatrix}\\ &= \begin{bmatrix}1&0&0&-1\\0&1&1&0\\1&0&0&1\\0&-1&1&0\end{bmatrix}\begin{bmatrix}\vec{e}_x\mathrm{LP}^{e}_{m,n}\\ \vec{e}_y\mathrm{LP}^{e}_{m,n}\\ \vec{e}_x\mathrm{LP}^{o}_{m,n}\\ \vec{e}_y\mathrm{LP}^{o}_{m,n}\end{bmatrix},\end{aligned} \tag{1}$$

where superscripts e and o represent the even and odd modes, $F_{m,n}(r)$ is the radial field distribution of the corresponding scalar mode (LP) solution, m is the azimuthal order of CVB modes, n is the radial order of CVB modes, r is the radial coordinate and φ is the angular coordinate. In optical fiber waveguides, hybrid electric (HE) and hybrid magnetic (EH) modes are two classes of hybrid electromagnetic modes that exhibit both longitudinal electric and magnetic field components ($E_z \neq 0$ and $H_z \neq 0$), distinguishing them from purely transverse electric (TE) or transverse magnetic (TM) modes. Note that $\mathrm{EH}^{e}_{m-1,n}$ is substituted by $\mathrm{TM}_{0,n}$ and $\mathrm{EH}^{o}_{m-1,n}$ is substituted by $\mathrm{TE}_{0,n}$ when $m = 1$.

Similarly, the OAM modes have a helical wave-front phase that can be formed by the superposition of CVB modes[40]. So, the OAM modes in the fiber can be expressed as a linear superposition of the odd and even CVB modes with $\pm\pi/2$ phase difference. Generally, in the weakly guiding fiber, the superposition of near-degenerate CVB modes forms LP states.

So, OAM modes can be expressed by the following:

$$\begin{aligned}\begin{bmatrix}\vec{\sigma}^{+}\mathrm{OAM}_{+m}\\ \vec{\sigma}^{-}\mathrm{OAM}_{-m}\\ \vec{\sigma}^{-}\mathrm{OAM}_{+m}\\ \vec{\sigma}^{+}\mathrm{OAM}_{-m}\end{bmatrix} &= F_{m,n}(r)\begin{bmatrix}\vec{\sigma}^{+}\exp(+jm\varphi)\\ \vec{\sigma}^{-}\exp(-jm\varphi)\\ \vec{\sigma}^{-}\exp(+jm\varphi)\\ \vec{\sigma}^{+}\exp(-jm\varphi)\end{bmatrix}\\ &= \begin{bmatrix}1&j&j&-1\\1&-j&-j&-1\\1&-j&j&1\\1&j&-j&1\end{bmatrix}\begin{bmatrix}\vec{e}_x\mathrm{LP}^{e}_{m,n}\\ \vec{e}_y\mathrm{LP}^{e}_{m,n}\\ \vec{e}_x\mathrm{LP}^{o}_{m,n}\\ \vec{e}_y\mathrm{LP}^{o}_{m,n}\end{bmatrix},\end{aligned} \tag{2}$$

where $\mathrm{OAM}_{\pm m}$ denotes the field distributions of helical wave-front phase $\exp(\pm jm\varphi)$; the subscripts '±' of OAM separately correspond to the left-hand and right-hand helical wave-front phases, respectively. In particular, the combination of LP modes with a $\pm\pi/2$ phase difference in the weakly guiding fiber can form LP OAM modes[41]:

$$\begin{aligned}\begin{bmatrix}\vec{e}_x\mathrm{OAM}_{-m}\\ \vec{e}_y\mathrm{OAM}_{-m}\\ \vec{e}_x\mathrm{OAM}_{+m}\\ \vec{e}_y\mathrm{OAM}_{+m}\end{bmatrix} &= F_{m,n}(r)\begin{bmatrix}\vec{e}_x\exp(-jm\varphi)\\ \vec{e}_y\exp(-jm\varphi)\\ \vec{e}_x\exp(+jm\varphi)\\ \vec{e}_y\exp(+jm\varphi)\end{bmatrix}\\ &= \begin{bmatrix}1&0&-j&0\\0&1&0&-j\\1&0&j&0\\0&1&0&j\end{bmatrix}\begin{bmatrix}\vec{e}_x\mathrm{LP}^{e}_{m,n}\\ \vec{e}_y\mathrm{LP}^{e}_{m,n}\\ \vec{e}_x\mathrm{LP}^{o}_{m,n}\\ \vec{e}_y\mathrm{LP}^{o}_{m,n}\end{bmatrix}.\end{aligned} \tag{3}$$

A schematic diagram of a programmable LP-mode synthesizer for CVB/OAM generation is illustrated in Figure 1, which interprets literally the mode conversion relations shown in Equations (1)–(3). Firstly, the LP-mode pool should be established to stock arbitrary LP modes and output them independently according to need. The flexible

https://doi.org/10.1017/hpl.2025.10060 Published online by Cambridge University Press

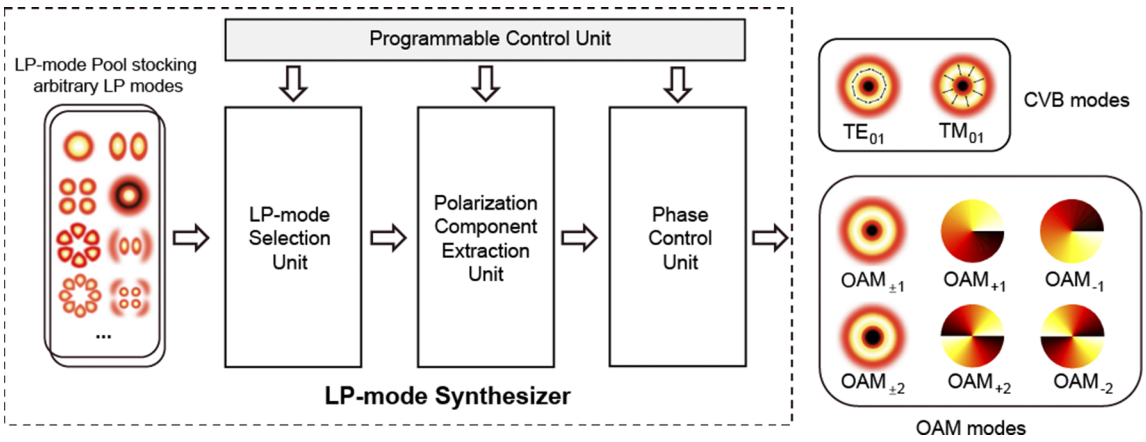


Figure 1. Schematic diagram of fiber-based CVB/OAM generation based on a programmable LP-mode synthesizer. The LP-mode pool based on weakly coupled FMF circuits generates independent and selectable LP modes. The LP-mode selection unit selects a specific LP mode and the polarization component extraction unit separates different polarization components, while the phase control unit adjusts the phase difference. All the operations could be controlled by the programmable control unit according to the mode conversion relations.

selection of an active LP mode in the LP-mode pool is made by the LP-mode selection unit. The polarization component extraction unit is used to detach the elements of the selected LP mode. After that, the phase differences among the elements are adjusted by the phase control unit. The programmable control unit is responsible for the configuration of the three units according to the conversion relations.

The physical implementations of the programmable LP-mode synthesizer may take flexible forms. The LP-mode pool accompanied with the LP-mode selection unit should output a switchable LP mode in a general way, which could be realized by various simple and effective approaches based on commercial optical components such as LP-mode converters or MMUXs. There are also different kinds of approaches for polarization component extraction and phase delay utilizing fiber-based or free-space micro-structured optical elements such as polarization beam splitters and optical delay lines. It should be noted that the optical circuit in the programmable LP-mode synthesizer should be built up based on weakly coupled FMFs and matched low modal crosstalk mode control components to sustain the independence among the LP modes.

3. Experimental setup

Figure 2 shows the experimental configuration of a fiber ring laser to verify the feasibility of the LP-mode synthesizer, the cavity of which is composed of both single-mode fiber (SMF) and FMF sections. Different types of laser structures could serve as the LP-mode synthesizer. In the experiment, we adopt the fiber ring laser for multiple merits of low mode competition, high stability and all-fiber structure. In the FMF section, the weakly coupled MRC FMF supports six LP modes, and the highest-order LP_{12} mode has large propagation loss and acts as a guarding mode, so independent light propagation can be achieved through five LP modes (LP_{01}, LP_{11}, LP_{21}, LP_{02}, LP_{31}) with very low modal crosstalk. The weakly coupled FMF enables multiple LP modes to oscillate independently. Single-mode instead of few-mode gain fiber is adopted, which could simplify the laser structure by eliminating the differential modal gain. The MMUX/MDEMUX may take flexible forms. In the experiment, we adopt cascaded MSCs. The MMUX/MDEMUX consists of five cascaded MSCs, and it should be noted that each MSC could only perform mode conversion between the fundamental mode in the SMF and one of a pair of degenerate LP modes in the FMF. The integration of weakly coupled FMF and matched MMUX/MDEMUX endows the system with the functionality of LP mode selection and control. An 80:20 few-mode optical coupler (FM-OC) is utilized as the output coupler of the laser, which is a free-space wave-plate beam splitter and achieves better mode insensitivity than a fused-type FM-OC[42]. A conventional single-mode pump scheme is adopted in the SMF section, consisting of 980-nm laser diode (LD), 980/1550-nm wavelength multiplexer (WMUX) for pump/signal light combination and a piece of single-mode erbium-doped fiber (SM-EDF) with the length of 5 m as the gain medium. The optical isolator (ISO) enables unidirectional light propagation. Single-mode optical coupler-1 (SM-OC-1) is used to split the light into five branches. The higher-order modes are converted back to LP_{01} mode by the MDEMUX and then combined to the SMF through SM-OC-2 for the next round of signal circulation.

The MRC-FMF in the experimental setup is a customized weakly coupled FMF fabricated by plasma chemical vapor deposition technique with the index profile as shown in Figure 3(a)[29], and the n_{eff} distribution at the wavelength of 1550 nm is also plotted. The FMF is designed to support weakly coupled mode division multiplexing transmission for six LP modes[29], for which the overall performance is

https://doi.org/10.1017/hpl.2025.10060 Published online by Cambridge University Press

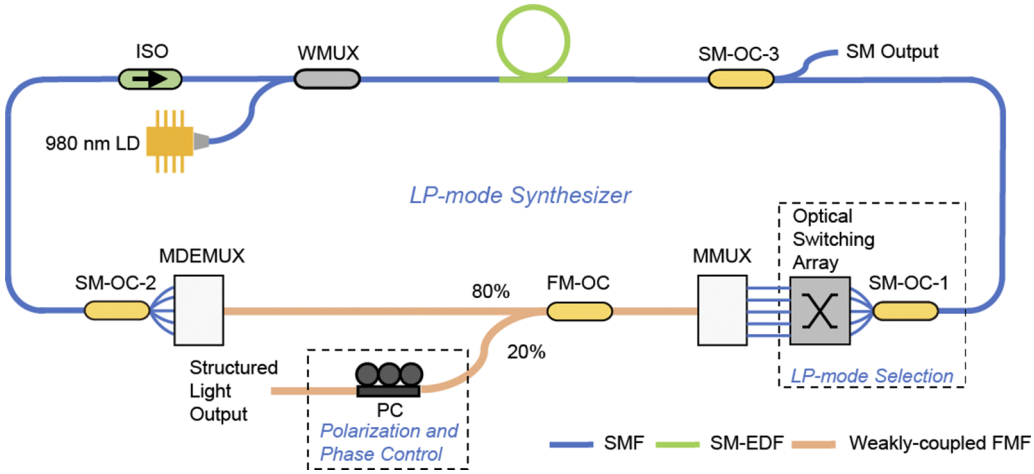


Figure 2. Experimental configuration of the proposed LP-mode synthesizer. The fiber ring laser based on partial weakly coupled FMF and related mode control components could output a switchable mode from five LP modes. Different CVB/OAM structured light could be generated by applying polarization and phase control utilizing the PC. WMUX, wavelength multiplexer; LD, laser diode; ISO, optical isolator, SM-EDF, single-mode erbium-doped fiber; SMF, single-mode fiber; SM-OC, single-mode optical coupler; MMUX, mode multiplexer; MDEMUX, mode demultiplexer; PC, polarization controller; FM-OC, few-mode optical coupler.

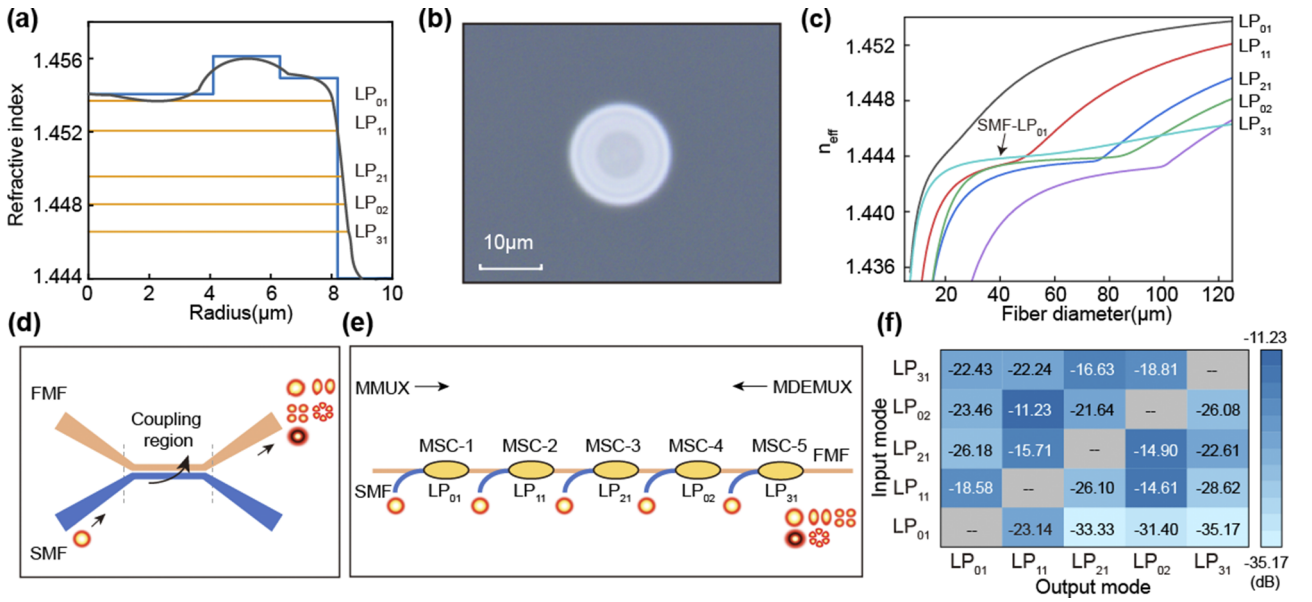


Figure 3. Design and fabrication of the weakly coupled MRC-FMF and MMUX/MDEMUX. (a) Designed (blue line) and measured (black line) index profiles of the fabricated weakly coupled FMF at the wavelength of 1550 nm. The effective indices of the supported LP modes are also shown. (b) Photo of the cross-section of the fabricated weakly coupled MRC-FMF. (c) Mode effective indices of LP_{01}, LP_{11}, LP_{21}, LP_{02} and LP_{31} modes in the designed FMF, and the LP_{01} mode in the SMF as a function of the fiber diameter after the tapering process. (d) Schematic structure of the MSC by tapering processes. (e) Schematic structures of the MMUX/MDEMUX composed of cascaded MSCs. (f) Measured modal-crosstalk among the five LP modes for back-to-back configuration.

limited by the worst mode channel with the largest modal crosstalk. Since the n_{eff} of all the LP modes lies between the indexes of the fiber core and cladding and the $|\Delta n_{\mathrm{eff}}|$ is the dominant factor for modal crosstalk between LP modes, the best transmission performance could be achieved when the n_{eff} of all the LP modes is equally spaced. So, the weakly coupled MRC-FMF is designed by applying two index perturbation regions to the core area of an initial step-index FMF to enlarge the minimum $|\Delta n_{\mathrm{eff}}|$ among all LP modes. The minimum $|\Delta n_{\mathrm{eff}}|$ of the weakly coupled MRC-FMF is 1.49×10^{-3}, lying between the LP_{21} and LP_{02} modes. The diameters of the central low-index region, the upper boundary of the high-index region, the fiber core and the cladding are 8.05, 12.45, 16.5 and 125 μm, respectively. The relative index differences for the core of the initial step-index FMF, the low-index region and the high-index region to the index of cladding are 0.748%, 0.688% and 0.827%, respectively. The normalized frequency V is 5.95 and six LP modes are contained in the weakly coupled MRC-FMF, among which the highest-order LP_{12} mode has a large

https://doi.org/10.1017/hpl.2025.10060 Published online by Cambridge University Press

propagation loss and acts as a guarding mode. A photo of the cross-section of the fabricated fiber is shown in Figure 3(b).

The matched MMUX and MDEMUX have the same structure composed of five cascaded MSCs but operate in opposite directions, as shown in Figure 3(e). Each MSC performs mode conversion between the fundamental mode of SMF and a specific LP mode in the MRC-FMF. The MSCs are fabricated by tapering parallel-placed MRC-FMF and SMF-28e fiber using a fused biconical taper platform (OSCOM, XQ-LZJ-B02) according to the phase-matching condition[43], as shown in Figure 3(d). At the coupling region, light from the SMF could be coupled to a specific LP mode with high selectivity. Figure 3(c) illustrates the changes of n_{eff} for tapered SMF and MRC-FMF with different fiber diameters. The phase-matching conditions could be satisfied at the cross-points in the curves, for which the corresponding values on the x-axis are the proper diameters for the tapered fibers. Different pre-tapering lengths for the MRC-FMF or the SMF should be applied to fabricate different MSCs. We can see that the n_{eff} of the LP_{01} mode in FMF is consistently higher than that of the LP_{01} mode in SMF. Therefore, pre-tapering the FMF is necessary for the LP_{01} MSC, while the SMF needs to be pre-tapered for the other MSCs.

The manufacturing of the MSCs involves two steps: pre-tapering the SMF or FMF to establish the initial diameter ratio of the two fibers, and then tapering the two fibers together, maintaining the diameter ratio constant. The two fibers are heated using a hydroxide flame. Continuous-wave light at 1550 nm is injected into the SMF, and the power and mode field pattern at the FMF output should be monitored during the second tapering process. The process is stopped when the output coupling power reaches its first maximum value. After the tapering process, the coupling region is pre-sealed and placed in a quartz groove, with the two ends fixed using thermosetting glue. Finally, a heat shrink tube is placed on the outer side of the quartz groove and heated to shrink it.

The modal crosstalk matrix of the MMUX/MDEMUX in back-to-back configuration is also measured. In this configuration, the MMUX and MDEMUX are connected directly without passing any component. The mode crosstalk is measured by injecting 0-dBm optical power at 1550 nm into the input port of the MMUX and measuring the optical power at each output port of the MDEMUX. For a five-LP mode MMUX/MDEMUX, the result is a 5×5 matrix with the diagonal elements being none, and each of the remaining elements is calculated by the ratio of the measured output power of each LP mode to that of the target LP mode. The modal crosstalk for all five modes can be less than –11.23 dB, as shown in Figure 3(f). The mode insertion losses of the MMUX/MDEMUX are also measured. For the insertion loss measurement of the MMUX, each time the probe light is injected into one single-mode input port of the cascaded five MSCs shown in Figure 3(e), the output power at the output FMF port is detected. For the insertion losses measurement of the MDEMUX, each time the MMUX is utilized to generate probe light for one of the five LP modes, the output power at the corresponding SMF output port is measured. For MMUX, the insertion losses of the LP_{01}, LP_{11}, LP_{21}, LP_{02} and LP_{31} modes are 0.61, 2.48, 4.43, 4.84 and 7.01 dB, respectively. For the MDEMUX, the insertion losses of the five modes are 0.76, 2.61, 4.25, 4.42 and 7.21 dB, respectively.

Compared with the schematic diagram of the LP-mode synthesizer shown in Figure 1, we can see that the whole fiber ring laser could act as the LP-mode pool with selectable output light from one of the five LP modes, while SM-OC-1 and the optical switching array (iseelink, GP-OSW1x16-SM-DT-FP) could bear the function of the LP-mode selection unit. Because the output of the fiber ring laser is not polarization-maintained, we adopt a PC for polarization and phase control, which is realized by coiling a certain number of loops of MRC-FMF around a three-paddle adjusting device. Each paddle could induce a fixed phase difference between polarization eigenmodes[44]. For the operation to non-degenerate LP_{mn} ($m = 0$) modes (e.g., LP_{01}, LP_{02} modes), the PC is employed to modify the polarization components and apply phase difference between them by twisting the three paddles to reallocate and select electric fields. While for the case of operation to degenerate LP_{mn} ($m \geq 1$) modes (e.g., LP_{11}, LP_{21} and LP_{31} modes), stress-induced birefringence in the PC can reallocate the optical power and apply phase difference among all four-fold eigenmodes even if only the even or odd mode is excited by the MMUX consisting of spatial-orientation-selective MSCs[44]. Therefore, the PC provides the functions of both polarization and phase control and is manually controlled. The output of the 3-dB SM-OC-3 as a reference Gaussian beam is utilized to verify the generation of OAM lasing. The spectrum properties of the laser are measured by an optical spectrum analyzer (Yokogawa, AQ6370C) with a resolution of 0.02 nm. The output mode profiles are observed by a charge-coupled device (CCD) camera (Xenics, Bobcat-5316). The output power is measured by an optical power-meter (EXFO, FPM-302X-FOA-22).

4. Experimental results

4.1. Experimental results for LP mode generation

The independent lasing for each LP mode of the proposed fiber ring laser is first investigated. The optical switching array is adjusted to excite each LP mode one by one, and the output power characteristics of output light at the 20% output port of the FM-OC are measured by the optical power-meter, while the intensity profile is measured by the CCD camera. The output signal power versus the pump power for five lasing modes is plotted in Figure 4(a). We can see that

https://doi.org/10.1017/hpl.2025.10060 Published online by Cambridge University Press

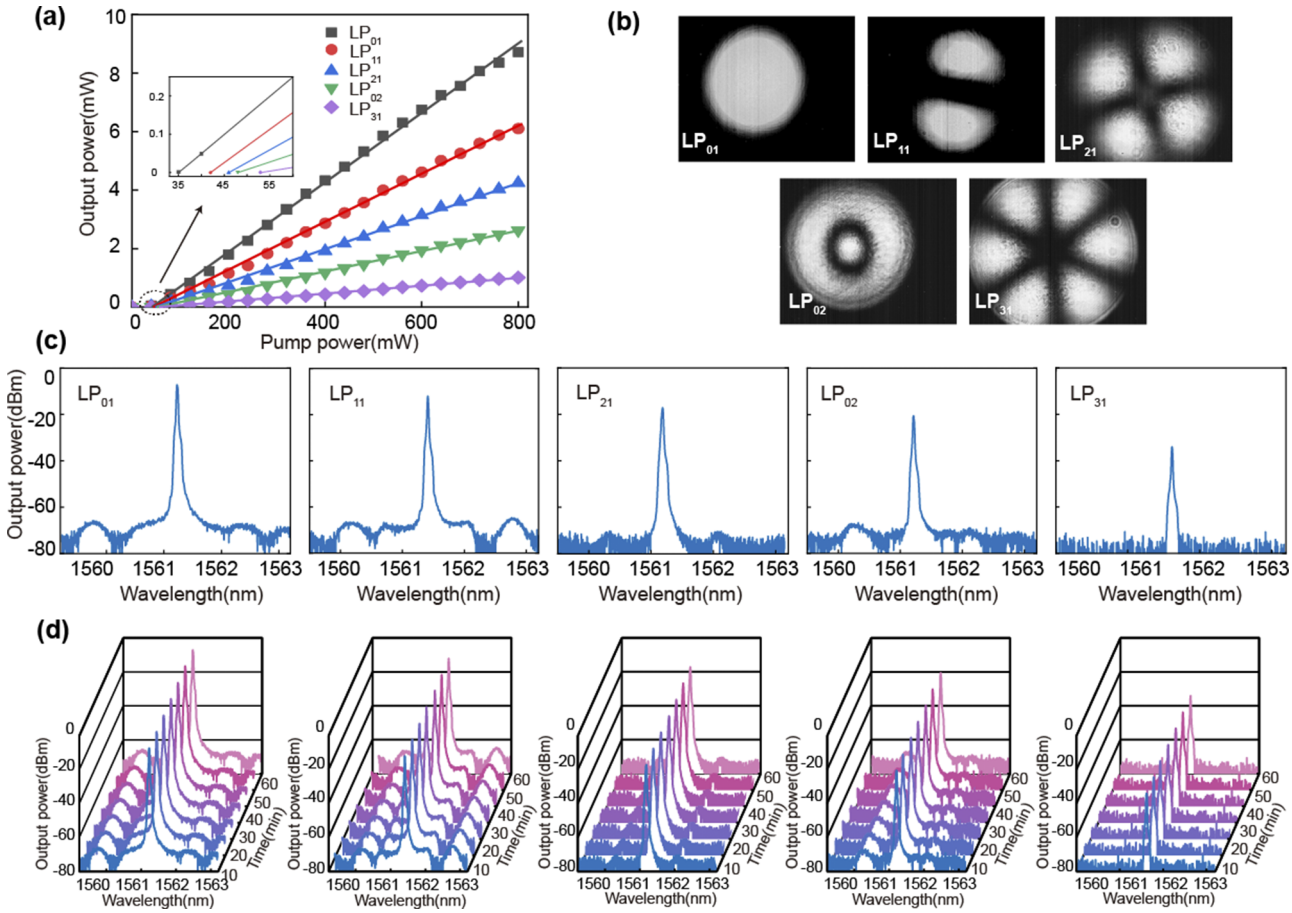


Figure 4. Experimental results of LP mode generation. (a) The relationship between the measured output power (dots) and the pump power for all five LP modes, and the linear fit (lines) suggests the slope efficiency for each mode. The inset shows the detailed plot when the pump power is in the range of 33–60 mW. (b) Intensity distributions for all five LP modes. (c) Optical spectra of all five LP modes at the fixed pump power of about 400 mW. (d) Output stabilities (repeated scan) for all five LP modes.

the lasing output power for different LP modes increases linearly with the pump power when working above the lasing threshold. The slope efficiencies of 1.17%, 0.82%, 0.56%, 0.35% and 0.13% and the pump power thresholds of 35, 42, 46, 48 and 53 mW are obtained for LP_{01}, LP_{11}, LP_{21}, LP_{02} and LP_{31} lasing modes, respectively. The different values of slope efficiencies and pump power thresholds among the five LP lasing modes are mainly influenced by different insertion losses for the five LP modes in the partial weakly coupled FMF cavity. Higher slope efficiency can be achieved by reducing the insertion losses of the optical components, especially those of the MMUX/MDEMUX. The intensity distributions of the LP modes are also recorded by the CCD camera, and the results are shown in Figure 4(b).

The spectral features and the stabilities of the lasing outputs are also investigated. Figure 4(c) shows the optical spectra of the lasing output of five LP modes measured by the optical spectrum analyzer when the pump power is fixed to be about 400 mW. The central wavelengths of 1561.23, 1561.41, 1561.18, 1561.25 and 1561.62 nm, the 3-dB linewidths of 0.028, 0.02, 0.028, 0.024 and 0.024 nm and the side-mode suppression ratios (SMSRs) of 59, 53, 53, 46 and 37 dB are achieved for the five LP modes from low to high orders, respectively. The wavelength differences come from the different effective lengths of lasing cavities for different LP modes. The residual spectra in the LP_{01} and LP_{11} may arise from nonideal coupling of energy into adjacent modes at specific wavelengths during LP mode selection. The output stabilities for the five lasing LP modes are measured during the 60-min period at room temperature, and the output optical spectra are shown in Figure 4(d). The data are recorded at 5-min intervals over a 60-min period. The fluctuations of peak wavelength and average output power for each lasing LP mode are less than 0.032 nm and 0.055 mW, respectively.

4.2. Experimental results for CVB generation

Selectable generation of CVBs is demonstrated utilizing the proposed LP-mode synthesizer. According to the conversion relationship between LP modes and CVB modes in Equation (1), the LP_{11} mode is formed by the

https://doi.org/10.1017/hpl.2025.10060 Published online by Cambridge University Press

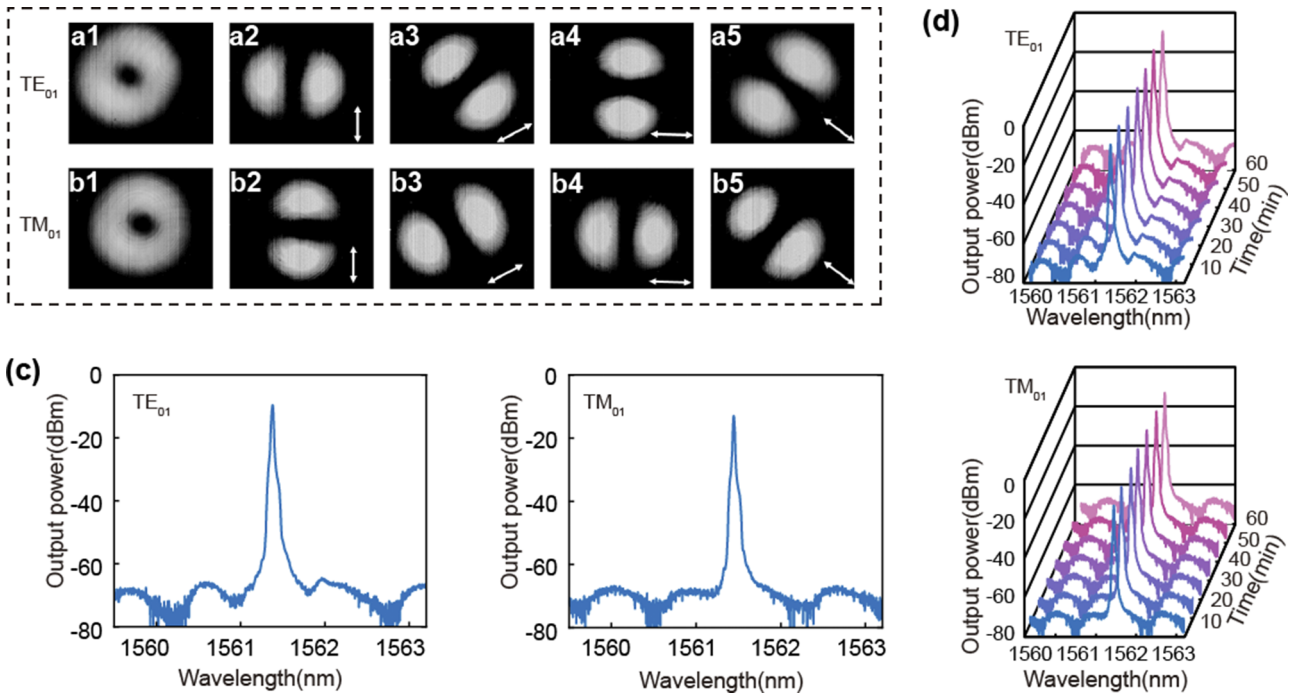


Figure 5. Experimental results of CVB mode generation. (a), (b) Measured intensity distributions before and after passing linear polarizers of TE_{01} and TM_{01}, respectively. The white arrows indicate the orientation of the linear polarizer. (c) Optical spectra of TE_{01} and TM_{01} outputs at the fixed pump power of about 400 mW. (d) Output stabilities (repeated scan) for TE_{01} and TM_{01} lasing modes at a 5-min interval during the 60-min period.

superposition of near-degenerate CVB modes including azimuthally polarized TE_{01}, radially polarized TM_{01}, and HE^{e}_{21}/HE^{o}_{21} modes. So, adjusting the optical switching array to only enable the lasing of LP_{11} modes, and then adjusting the PC to induce the rotation and extrusion, we could obtain the TE_{01} or TM_{01} mode. The intensity distributions of the output light are recorded by the CCD camera, and the results are shown in Figures 5(a) and 5(b). Figures 5(a1) and 5(b1) show the doughnut-shaped intensity profiles of both the TE_{01} and TM_{01} modes, respectively. In order to distinguish the polarization distributions of both CVB modes, a rotatable linear polarizer is placed in the light path between the lasing output and the CCD camera. Figures 5(a2)–5(a5) and 5(b2)–5(b5) show the intensity distributions with different polarization orientations (represented with white arrows) for the polarizer. The intensity patterns with a two-lobe shape perpendicular to the orientation of the linear polarizer in Figures 5(a2)–5(a5) show that the output lasing beam is in azimuthally polarized TE_{01} mode, while the intensity patterns with the two-lobe shape parallel to the orientation of the linear polarizer in Figures 5(b2)–5(b5) indicate that the light beam is radially polarized TM_{01} mode.

Figure 5(c) presents the optical spectra of CVB outputs at the fixed pump power of about 400 mW. The central wavelengths of 1561.38 and 1561.45 nm, the 3-dB linewidths of 0.024 and 0.024 nm and the SMSRs of 55 and 54 dB are measured for the TE_{01} and TM_{01} lasing modes, respectively. Figure 5(d) shows the output stabilities for TE_{01} and TM_{01} lasing modes at a 5-min interval during the 60-min period. The peak wavelength fluctuation and the average output power fluctuation for the TE_{01} lasing mode are less than 0.044 nm and 0.042 mW, respectively. The fluctuations of peak wavelength and average output power for the TM_{01} lasing mode are less than 0.040 nm and 0.030 mW, respectively.

4.3. Experimental results for OAM generation

Selectable generation of OAMs is also verified utilizing the proposed LP-mode synthesizer. According to the conversion relationship in Equation (3), the LP OAMs can be obtained by the superposition of a specific pair of degenerate LP modes in the weakly guiding FMF under proper polarization and phase control. For example, $\vec{e}_x \mathrm{OAM}_{\pm m} = \vec{e}_x \mathrm{LP}^{e}_{m,1} \pm \vec{e}_x j\mathrm{LP}^{o}_{m,1}$, which means that the *x*-polarized OAM modes can be obtained by combining the even and odd $LP_{m,1}$ modes having the same polarized direction with a $\pm\pi/2$ phase shift. The $OAM_{\pm1}$ could be obtained utilizing the $LP^{e}_{1,1}$ and $LP^{o}_{1,1}$, while the $OAM_{\pm2}$ could be obtained utilizing the $LP^{e}_{2,1}$ and $LP^{o}_{2,1}$. So, the optical switching array should be adjusted to obtain the LP_{11} or LP_{21} lasing output for the generation of the $OAM_{\pm1}$ or $OAM_{\pm2}$, respectively. Then, the corresponding OAM beams will be obtained by tuning the PC's rotation angle and stress to induce the phase difference of $\pi/2$ between even and odd modes. Figure 6(a) shows the interference setup used to determine the topological charge number (±1, ±2) of the generated OAM beams by observing their

https://doi.org/10.1017/hpl.2025.10060 Published online by Cambridge University Press

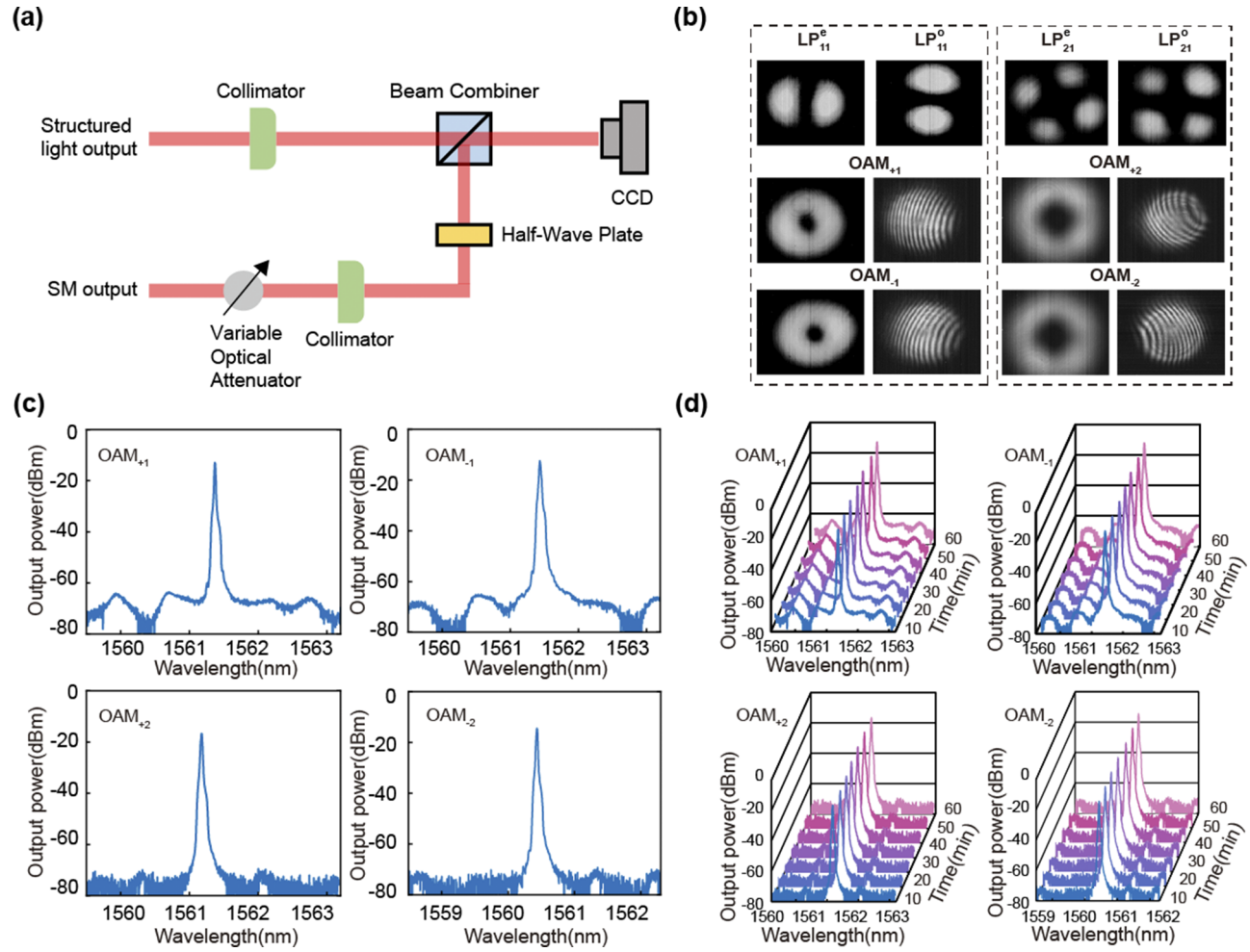


Figure 6. Experimental results for OAM mode generation. (a) Interference setup for characterizing the generated OAM beams. (b) Measured intensity distributions and fork intensity patterns at the laser output. Row 1 shows the intensity profiles of LP^{e}_{11}, LP^{o}_{11}, LP^{e}_{21} and LP^{o}_{21}; rows 2 and 3 represent the OAM modes with different topological charges and their responding interference patterns, respectively. (c) Optical spectra of OAM_{+1}, OAM_{-1}, OAM_{+2} and OAM_{-2} outputs at the fixed pump power of about 400 mW. (d) Output stabilities (repeated scan) for all four lasing OAM modes.

characteristic fork patterns with a CCD camera. The reference Gaussian beam at the output of SM-OC-3 is used for the interference setup to analyze the generated OAM beams. A free-space beam combiner combines both lights to form the interference pattern and a variable optical attenuator balances the power of the two optical paths. A half-wave plate is used to adjust the polarization state of the reference Gaussian beam. By properly adjusting the PC, annular intensity profiles and their corresponding patterns could be observed. Figure 6(b) presents the measured intensity distributions for LP modes and OAM beams and fork intensity patterns at the laser output. The number of forks represents the topological charge of the OAM beams, which is $|m| = 1, 2$.

Figure 6(c) shows the optical spectra of the OAM_{+1}, OAM_{-1}, OAM_{+2} and OAM_{-2} outputs at the fixed pump power of about 400 mW. The central wavelengths of 1561.39, 1561.43, 1561.18 and 1560.44 nm, the 3-dB linewidths of 0.020, 0.028, 0.032 and 0.028 nm and the SMSRs of 51, 53, 53 and 55 dB are measured for the OAM_{+1}, OAM_{-1}, OAM_{+2} and OAM_{-2} lasing modes, respectively. Figure 6(d) shows the output stabilities for all four OAM lasing modes at a 5-min interval during the 60-min period. The fluctuations of peak wavelength for the OAM_{+1}, OAM_{-1}, OAM_{+2} and OAM_{-2} lasing modes are less than 0.048, 0.056, 0.072 and 0.060 nm, respectively, while the fluctuations of average output power are 0.072, 0.060, 0.041 and 0.058 mW, respectively.

5. Conclusion

In summary, we have proposed the concept of a programmable LP-mode synthesizer as a general way to generate CVB/OAM structured light according to their conversion relationship with LP modes. Based on a compact fiber ring laser generating switchable one of five LP modes and a PC for polarization and phase control, we successfully demonstrate the feasibility of the LP-mode synthesizer with

https://doi.org/10.1017/hpl.2025.10060 Published online by Cambridge University Press

the generation of TE_{01}, TM_{01}, OAM_{+1}, OAM_{-1}, OAM_{+2} and OAM_{-2} modes. Although the MMUX/MDEMUX will introduce additional insertion losses, it allows precise mode control of output light, which will greatly benefit high-power structured light applications. The programmable capability for the LP-mode synthesizer could be further realized by applying polarization-maintaining structures to the LP-mode pool. The mode purity of the generated structured light could be monitored to improve the beam quality. The scheme may be further extended to other types of structured light, such as Bessel beams. The proposed programmable synthesizer could take full advantage of mature LP mode manipulation schemes based on weakly coupled FMFs and related optical components and is promising to be extended to wide applications.

Acknowledgment

This work was supported by the National Natural Science Foundation of China (Grant No. U20A20160,62101009) and the Peng Cheng Zili Project (Grant No. PCL2023AS2-4).

References

1. B. J. Puttnam, G. Rademacher, and R. S. Luís, Optica **8**, 1186 (2021).
2. G. B. Xavier and G. Lima, Commun. Phys. **3**, 9 (2020).
3. G. Milione, T. Wang, J. Han, and L. Bai, Chin. Opt. Lett. **15**, 030012 (2017).
4. F. Pang, L. Xiang, H. Liu, L. Zhang, J. Wen, X. Zeng, and T. Wang, J. Lightwave Technol. **39**, 3740 (2021).
5. B. M. Heffernan, P. S. Riley, O. D. Supekar, S. A. Meyer, D. Restrepo, M. E. Siemens, E. A. Gibson, and J. T. Gopinath, APL Photonics **7**, 036102 (2022).
6. Z. H. Qian, J. M. Cui, X. W. Luo, Y. X. Zheng, Y. F. Huang, M. Z. Ai, R. He, C. F. Li, and G. C. Guo, Phys. Rev. Lett. **127**, 263603 (2021).
7. Y. Li, L. M. Zhou, and N. Zhao, Opt. Lett. **46**, 106 (2021).
8. M. Padgett and R. Bowman, Nat. Photonics **5**, 343 (2011).
9. A. S. Ostrovsky, C. Rickenstroff-Parrao, and V. Arrizón, Opt. Lett. **38**, 534 (2013).
10. Z. Y. Rong, Y. J. Han, S. Z. Wang, and C. S. Guo, Opt. Express **22**, 1636 (2014).
11. L. Li, X. Zheng, C. Jin, M. Qi, X. Chen, Z. Ren, J. Bai, and Z. Sun, Appl. Phys. Lett. **105**, 221103 (2014).
12. Y. Xiang, S. Bai, and Z. Zhang, Opt. Laser Technol. **160**, 109079 (2023).
13. D. Naidoo, F. S. Roux, A. Dudley, I. Litvin, B. Piccirillo, L. Marrucci, and A. Forbes, Nat. Photonics **10**, 327 (2016).
14. G. Milione, H. I. Sztul, D. A. Nolan, J. Kim, M. Etienne, J. McCarthy, J. Wang, and R. R. Alfano, in *CLEO* (Optica Publishing Group, 2011), paper CTuB2.
15. M. W. Beijersbergen, R. P. Coerwinkel, M. Kristensen, and J. P. Woerdman, Opt. Commun. **112**, 321 (1994).
16. S. Oemrawsingh, J. Houwelingen, E. Eliel, J. P. Woerdman, E. Verstegen, J. G. Kloosterboer, and G. Hooft, Appl. Opt. **43**, 688 (2004).
17. J. Feng, H. Shi, J. Yi, A. Zhang, S. Burokui, J. Chen, X. Chen, and Z. Xu, Phys. Rev. Appl. **19**, 044075 (2023).
18. E. Karimi, S. Schulz, I. Leon, H. Qassim, J. Upham, and R. Boyd, Light Sci. Appl. **3**, e167 (2014).
19. H. Ahmed, H. Kim, Y. Zhang, Y. Intaravanne, J. Jang, J. Rho, S. Chen, and X. Chen, Nanophotonics **11**, 941 (2022).
20. C. Li, T. Wieduwilt, F. J. Wendisch, A. Márquez, L. S. Menezes, S. A. Maier, M. A. Schmidt, and H. Ren, Nat. Commun. **14**, 7222 (2023).
21. W. Chang, M. Feng, B. Mao, P. Wang, Z. Wang, and Y. Liu, J. Lightwave Technol. **40**, 4804 (2022).
22. C. Jiang, K. Zhou, B. Sun, Y. Wan, Y. Ma, Z. Wang, Z. Zhang, C. Mou, and Y. Liu, Opt. Lett. **48**, 2965 (2023).
23. J. Lv, J. Lin, X. Ma, C. Dai, C. Gu, P. Yao, L. Xu, and Q. Zhan, Opt. Express **30**, 18320 (2022).
24. Z. Xie, S. Gao, T. Lei., S. Feng, Y. Zhang, F. Li, J. Zhang, Z. Li, and X. Yuan, Photonics Res. **6**, 743 (2018).
25. M. Zhang, J. Wen, Y. Wu, Y. Cao, Y. Luo, X. Zhang, F. Pang, W. Chen, and T. Wang, IEEE Photonics J. **15**, 7201907 (2023).
26. H. Wan, J. Wang, Z. Zhang, J. Wang, S. Ruan, and L. Zhang, J. Lightwave Technol. **36**, 3403 (2018).
27. D. Mao, Z. He, H. Lu, M. Li, W. Zhang, X. Cui, B. Jiang, and J. Zhao, Opt. Lett. **43**, 1590 (2018).
28. D. Soma, S. Beppu, Y. Wakayama, K. Igarashi, T. Tsuritani, I. Morita, and M. Suzuki, J. Lightwave Technol. **36**, 1375 (2018).
29. D. Ge, Y. Gao, Y. Yang, L. Shen, Z. Li, Z. Chen, Y. He, and J. Li, Opt. Commun. **451**, 97 (2019).
30. M. Zuo, D. Ge, J. Liu, Y. Gao, L. Shen, X. Lan, Z. Chen, Y. He, and J. Li, Opt. Express **30**, 5868 (2022).
31. B. Huang, N. K. Fontaine, R. Ryf, B. Guan, S. G. Leon-Saval, R. Shubochkin, Y. Sun, R. Lingle, and G. Li, Opt. Express **23**, 224 (2015).
32. S. G. Leon-Saval, N. K. Fontaine, J. R. Salazar-Gil, B. Ercan, R. Ryf, and J. Bland-Hawthorn, Opt. Express **22**, 1036 (2014).
33. G. Labroille, B. Denolle, P. Jian, P. Genevaux, N. Treps, and J. Morizur, Opt. Express **22**, 15599 (2014).
34. G. Labroille, P. Jian, N. Barré, B. Denolle, and J. Morizur, in *Optical Fiber Communication Conference* (Optica Publishing Group, 2016), paper Th3E.5.
35. K. Aoki, A. Okamoto, Y. Wakayama, A. Tomita, and S. Honma, Opt. Lett. **5**, 769 (2013).
36. J. Cui, Y. Gao, S. Huang, J. Yu, J. Liu, J. Jia, Y. He, Z. Chen, and J. Li, J. Lightwave Technol. **41**, 2991 (2023).
37. Y. Gao, J. Cui, D. Ge, J. Jia, C. Du, C. Xia, Y. Liu, Z. Li, Y. He, Z. Chen, J. Li, and G. Li, J. Lightwave Technol. **37**, 4410 (2019).
38. Q. Zhan, Adv. Opt. Photonics **1**, 1 (2009).
39. L. Allen, M. W. Beijersbergen, R. Spreeuw, and J. P. Woerdman, Phys. Rev. A **45**, 8185 (1992).
40. S. Ramachandran and P. Kristensen, Nanophotonics **2**, 455 (2013).
41. Y. Han, Y. G. Liu, W. Huang, Z. Wang, J. Guo, and M. Luo, Opt. Express **24**, 17272 (2016).
42. F. Ren, X. Huang, and J. Wang, Opt. Eng. **56**, 116101 (2017).
43. R. Ismaeel, T. Lee, B. Oduro, Y. Jung, and G. Brambilla, Opt. Express **22**, 11610 (2014).
44. H. C. Lefèvre, Electron. Lett. **16**, 778 (1980).

https://doi.org/10.1017/hpl.2025.10060 Published online by Cambridge University Press